

RESEARCH ARTICLE | SEPTEMBER 28 2022

## Effects of wedge-angle change on the evolution of oblique detonation wave structure

Jie Sun (孙杰)  ; Pengfei Yang (杨鹏飞)   ; Baolin Tian (田保林)  ; Zheng Chen (陈正) 



*Physics of Fluids* 34, 096112 (2022)  
<https://doi.org/10.1063/5.0102842>

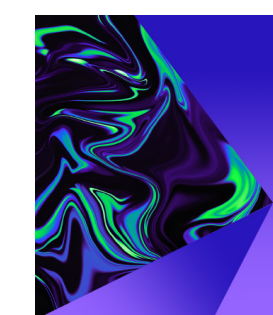


View  
Online



Export  
Citation

CrossMark



## Physics of Fluids

Special Topic:  
Selected Papers from the 2023 Non-Newtonian  
Fluid Mechanics Symposium in China

**Submit Today**



# Effects of wedge-angle change on the evolution of oblique detonation wave structure

Cite as: Phys. Fluids 34, 096112 (2022); doi: 10.1063/5.0102842

Submitted: 13 June 2022 · Accepted: 2 September 2022 ·

Published Online: 28 September 2022



View Online



Export Citation



CrossMark

Jie Sun (孙杰),<sup>1</sup> Pengfei Yang (杨鹏飞),<sup>1,a)</sup> Baolin Tian (田保林),<sup>1,2</sup> and Zheng Chen (陈正)<sup>1</sup>

## AFFILIATIONS

<sup>1</sup>CAPT, SKLTCS, College of Engineering, Peking University, Beijing 100871, China

<sup>2</sup>LCP, Institute of Applied Physics and Computational Mathematics, Beijing 100094, China

<sup>a)</sup>Author to whom correspondence should be addressed: young1505@foxmail.com

## ABSTRACT

Compared to pulse detonation engine and rotating detonation engine, oblique detonation engine has the advantage of higher flight Mach number. However, it is still challenging to achieve stabilized oblique detonation wave for a broad range of flight conditions. To control oblique detonation wave, this study focuses on the oblique detonation wave structure evolution induced by changing the wedge angle. Transient two-dimensional simulations are conducted for wedge-stabilized oblique detonation wave in a stoichiometric hydrogen/air mixture. The detailed chemistry of hydrogen combustion is considered, and the thermal states of the reactants are determined by the specified flight altitude and the Mach number. The angle change between inflow and wedge can be achieved in two ways: inflow-angle change with fixed wedge angle and wedge-angle change with fixed inflow direction. Results indicate that no new autoignition zone exists in the transient wave evolution caused by wedge-angle change, which is different from that of inflow-angle change observed in previous studies. For the wedge-angle change process, the effects of wedge-angle change rate on transient oblique detonation wave structure evolution are further assessed. It is found that the transient oblique detonation wave structure is more sensitive to the wedge-rotation angular velocity for increasing wedge angle (controlled by the thermodynamic properties of the mixture) than that for decreasing wedge angle (controlled by the shock wave dynamic). For the quasi-steady triple-wave structure during wedge-angle decreasing process, a normal detonation wave occurs and becomes dominant in the wave structure evolution, whose formation mechanism is analyzed by the polar curve theory.

Published under an exclusive license by AIP Publishing. <https://doi.org/10.1063/5.0102842>

19 March 2024 03:31:41

## I. INTRODUCTION

Detonation has promising applications in hypersonic propulsion systems because of its high thermal efficiency and compact structure.<sup>1</sup> Currently, there are mainly three types of detonation engines: pulse detonation engine (PDE), rotating detonation engine (RDE), and oblique detonation engine (ODE).<sup>1–5</sup> In general, the PDE and RDE work at a relatively low operational Mach number, that is,  $Ma < 6$ , while ODE is particularly suitable for hypersonic flight<sup>6–8</sup> with the higher Mach number.

Li *et al.*<sup>9</sup> obtained the wedge-stabilized oblique detonation structure in simulations. They found that the oblique detonation wave (ODW) structure consists of a non-reactive oblique shock wave (OSW), an induction region, a group of deflagration waves, and an oblique detonation surface. Subsequently, extensive numerical and experimental studies were conducted for ODW with emphasis on the morphology of steady ODW.<sup>10–16</sup> For wedge-stabilized ODW, the transition pattern between the leading OSW and the main ODW can be categorized as smooth and abrupt transitions,<sup>16–18</sup> respectively. The

transition pattern depends upon the inflow Mach number, wedge angle, and mixture reactivity.<sup>11,16–21</sup> Smooth transition usually occurs for high flight Mach number and large attack angle, while the abrupt transition occurs in the opposite conditions.<sup>16,18</sup> Teng *et al.*<sup>13</sup> proposed a semi-theoretical method for predicting the ODW morphology based on geometric analysis. In addition, the semi-theoretical model also provides a reasonable explanation for the formation criterion of the smooth/abrupt ODW structure.

The preceding works mainly deal with the steady morphology of ODW. However, the unsteadiness of ODW due to the change in the reactant composition and velocity plays a crucial role in the operation of realistic engines. Liu *et al.*<sup>22</sup> found that the inflow-angle change can induce the hysteresis phenomenon in which double solutions were observed for the ODW structure under the same wedge angle and inflow parameters. Yang *et al.*<sup>23</sup> studied the unsteady ODW caused by periodic density/temperature disturbance of the inflow. They showed that the disturbance frequency has significant impact on the ODW structure and dynamics. Zhang *et al.*<sup>24</sup> numerically investigated the

transient ODW evolution caused by abrupt wedge-angle change. The results indicated that the ODW structure evolution between the “downstream process” and the “upstream process” is irreversible and that new ignition points appear before the original reaction front during the upstream process. Liu *et al.*<sup>22</sup> and Zhang *et al.*<sup>24</sup> assumed that the wedge-angle change is completely equivalent to the inflow-angle variation, and accordingly, the wedge remains unaltered but the inflow changes in their simulations. For a steady process, one can define a solid wedge rotation that makes these two problems equivalent mathematically. However, detonation evolution is a highly transient and multi-dimensional phenomenon in association with the vigorous chemical heat release rate, which make the flow details extremely complex. In such transient process, the historical variation of the flow configuration plays a decisive role in affecting the subsequent evolution and the route to the final state. Therefore, the effect of wedge-angle change rate essentially differs from that of flow angle variation rate on transient ODW development and therefore must be investigated individually.

The above-mentioned considerations constitute the motivation for the present study on the evolution of ODW structure induced by wedge-angle change. The aim of this study is twofold. First, the difference in the transient ODW evolution caused by wedge-angle change (WAC) and inflow-angle change (IAC) is interpreted via separate controlled mechanisms. Second, the transient ODW structure evolutions during the WAC process are assessed with emphasis on the dynamic properties of newly formed normal detonations in the initiation zone. In this work, the wedge-stabilized ODW in a stoichiometric hydrogen/air mixture is simulated, in which the thermal states of the unburned mixture are chosen according to the specified flight altitude and flight Mach number.<sup>13</sup> In the simulations, the dynamic mesh technique is employed in order to achieve the wedge-angle change.

The paper is organized as follows. The formulation and numerical methods are introduced in Sec. II. Then, typical transient ODW structure evolution caused by WAC and, moreover, the effects of angular velocity in WAC are examined in Sec. III. The concluding remarks are presented in Sec. IV.

## II. MODEL AND NUMERICAL METHODS

Transient two-dimensional simulations are conducted to solve the wedge-stabilized ODW. The schematics and computational domain are shown in Fig. 1. The computational domain is  $-0.5 \leq x \leq 5$  cm and

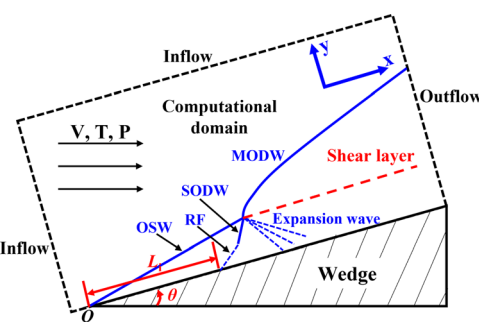


**FIG. 1.** Schematic of wedge-induced ODW and simulation settings. RF: reaction front; SODW: secondary oblique detonation wave; and ODW: oblique detonation wave.

$0 \leq y \leq 2.5$  cm. The wedge starts from  $x = y = 0$  cm. Supersonic inflow condition is imposed at the top and left boundaries, and supersonic outflow conditions are implemented on the right boundary. For the bottom boundary, the outflow boundary is used in the range of  $-0.5 \leq x < 0$  cm. To investigate the effects of wedge-angle change, a dynamic mesh method offered by OpenFOAM official<sup>25</sup> is used in the remaining region with  $0 \leq x \leq 5$  cm. The dynamic mesh library of OpenFOAM as an independent module has been introduced and verified in Jasak's work.<sup>26</sup> By means of the *movingWallVelocity* boundary condition, the wedge-angle change with finite angular velocity can be realized.

The wall is assumed to move around O-point at constant angular velocity  $\omega$ . For the bottom grid nearest the moving wall whose distance from O-point is  $L$ , the normal velocity of the flow to the wedge should equal to the moving wall, that is,  $\omega \cdot L$ , which can prevent the fluid leakage from the moving wall surface when dynamic mesh is used for varying wedge angle. The tangent velocity along the moving wall is determined according to the zero-gradient condition for inviscid flow. In realistic ODE, the change of the inflow direction is usually caused by the adjustment of air intake compression angle, which is a predetermined entrance condition for the wedge-induced ODW. Thus, the external force causing the inflow-angle change is not considered in the present study. Following previous studies,<sup>22,24</sup> the inflow angle is directly changed by modifying the left inflow conditions with time; that is, the increment/decrement of the inflow angle should satisfy  $\Delta\theta = \omega \cdot t$ , where  $\theta$  is the angle of the wedge,  $\omega$  the angular velocity of its rotation, and  $t$  the time. The dynamic mesh is used to simulate the wedge movement due to external transmission. For simplicity, the inflow/wedge angle is assumed to alter uniformly at constant angular velocity.

As shown in Fig. 1, the inflow imposes on the wedge surface with angle  $\theta$ . The ignition length,  $L_p$ , is defined as the distance from the leading edge to the position where autoignition first occurs on the wedge surface. The position of autoignition is defined as the location on the wedge where the maximum heat release is achieved. The inflow states are specified as  $P = 196.3$  kPa,  $T = 814.4$  K, and  $V = 2418.9$  m/s are used in the simulations, which are calculated based on the specified flight altitude,  $H_0 = 20$  km, and flight Mach number,  $M_0 = 9$ , according to Teng *et al.*<sup>13</sup> The inflow is the stoichiometric hydrogen/air mixture. A detailed hydrogen reaction mechanism including 13 species and 27 reactions<sup>27</sup> is used to mimic the combustion process, which has been applied widely in hydrogen combustion simulations.<sup>13,28</sup>

The transient two-dimensional ODW evolution caused by WAC and IAC is simulated using the solver, *detonationFoam*, developed based on OpenFOAM.<sup>25</sup> OpenFOAM is an open-source frame and has been successfully in simulating combustion phenomena.<sup>29–31</sup> Existing studies<sup>32,33</sup> showed that the viscous boundary layer had little effects on the ODW initiation structure since it was extremely suppressed in hypersonic flow. Mazaheri *et al.*'s work<sup>34</sup> showed that the shock structures obtained by solving Euler and Navier-Stokes equations differ slightly for weakly irregular detonations. Hence, the following Euler governing equations for compressible, inviscid, multi-species, reactive flow are solved in this work. Therefore, the following Euler governing equations for compressible, inviscid, multi-species, reactive flow are solved in this work:

$$\begin{aligned} \frac{\partial \rho}{\partial t} + \frac{\partial(\rho u_i)}{\partial x_i} &= 0, \\ \frac{\partial(\rho u_i)}{\partial t} + \frac{\partial}{\partial x_j} (\rho u_i u_j) + \frac{\partial p}{\partial x_i} &= 0, \quad i = x, y, \\ \frac{\partial(\rho E)}{\partial t} + \frac{\partial}{\partial x_j} [(\rho E + p) u_j] &= 0, \\ \frac{\partial(\rho Y_k)}{\partial t} + \frac{\partial(\rho u_i Y_k)}{\partial x_i} &= \omega_k, \quad k = 1, \dots, N - 1. \end{aligned} \quad (1)$$

Here,  $Y_k$  is the mass fraction of the  $k$ th species,  $\omega_k$  is the production/consumption rate of the  $k$ th species, and  $N$  is the total number of species.

The thermodynamic properties of the species in detonationFoam are described according to the JANAF model.<sup>35</sup> The thermodynamic parameters, such as the specific heat capacity at constant pressure,  $C_p$ , and the enthalpy,  $h$ , are described as polynomials of the temperature. Corresponding coefficients and two polynomials separate for a lower and a higher temperature range are specified. In the JANAF model,  $C_p$  and  $h$  of species are defined as<sup>30</sup>

$$\frac{C_p}{R} = \sum_{n=0}^4 a_n T^n, \quad (2)$$

$$\frac{h}{RT} = \sum_{n=0}^4 \frac{a_n T^n}{n+1} + \frac{a_{n,5}}{T}, \quad (3)$$

where  $T$  is the temperature,  $R$  is the molar gas constant, and  $a_n$  is the auxiliary input parameters provided by the thermodynamic files. The reaction rate constant for elementary reactions is in the Arrhenius form<sup>36</sup>

$$K = AT^\beta e^{-\frac{E_a}{RT}}. \quad (4)$$

Here,  $E_a$  is the activation energy,  $A$  the pre-exponential factor, and  $\beta$  the temperature exponent. The reaction rate constant,  $K$ , is acquired to calculate the production/consumption rate of each species. These parameters are provided in the kinetic model.

The finite volume method is used in detonationFoam. The Strang splitting method<sup>37</sup> is adopted to solve the convection terms. The second-order MUSCL scheme<sup>38</sup> is used to reconstruct the face-centered values from the body-centered data, while the modified Riemann solver, HLLCP,<sup>39</sup> is used to calculate the convection fluxes. The Seulex ordinary differential equation solver<sup>40</sup> is used to solve the chemical reaction process. The first-order explicit Euler scheme is used for time advance. The dynamic mesh library provided by OpenFOAM official<sup>25</sup> is called to achieve the wedge rotation. By solving the Laplace equation of flow field deformation, the original flow field is mapped to the new domain after geometric change to simulate the effects of wedge rotation. Code validation is demonstrated in the Supplement Document, in which the simulation results for typical cases are shown.

To demonstrate the grid convergence and examine the reliability of the numerical simulation, the wedge-induced ODW with three grid sizes of  $\delta x = 20, 10$ , and  $5 \mu\text{m}$  is first simulated. Figure 2(a) shows the temperature contours of the ODW structure for grid sizes of  $\delta x = 10$  and  $\delta x = 5 \mu\text{m}$ . It is seen that the wave structures of ODW temperature fields are nearly the same for these two grid resolutions. In addition, quantitative comparison is conducted by plotting the pressure and temperature distributions along the line at  $y = 0.2 \text{ cm}$  in Fig. 2(b). The numerical results for grid sizes of  $\delta x = 10$  and  $5 \mu\text{m}$  are almost identical. Therefore, the grid resolution with  $\delta x = 10 \mu\text{m}$  is accurate enough to ensure the grid convergence and the uniform grid with  $\delta x = \delta y = 10 \mu\text{m}$  is used in all simulations. For the mixture of inflow, the induction length of its Zeldovich Neuman-Doring (ZND) structure is calculated as  $117.2 \mu\text{m}$  and there are more than ten grids in the induction region, which ensures the detonation wave structure can be adequately resolved.

### III. RESULTS AND DISCUSSION

#### A. Oblique detonation wave structure

The temperature and pressure contours of steady ODW structure with wedge angle of  $\theta = 18^\circ$  and  $24^\circ$  are obtained. Figure 3(a) shows

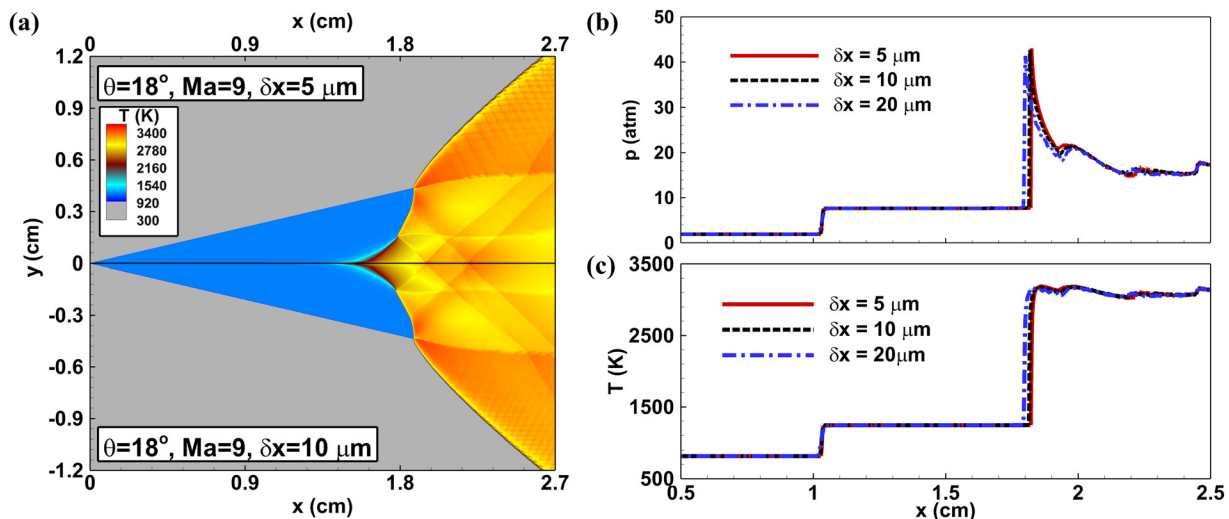


**FIG. 2.** Comparison of simulation results obtained from three grid sizes of  $\delta x = 20, \delta x = 10$ , and  $\delta x = 5 \mu\text{m}$  with  $\theta = 18^\circ$ . (a) The ODW temperature contours for  $\delta x = 5$  and  $\delta x = 10 \mu\text{m}$ . The pressure (b) and temperature (c) distributions along the line at  $y = 0.2 \text{ cm}$  for these three grid solutions.

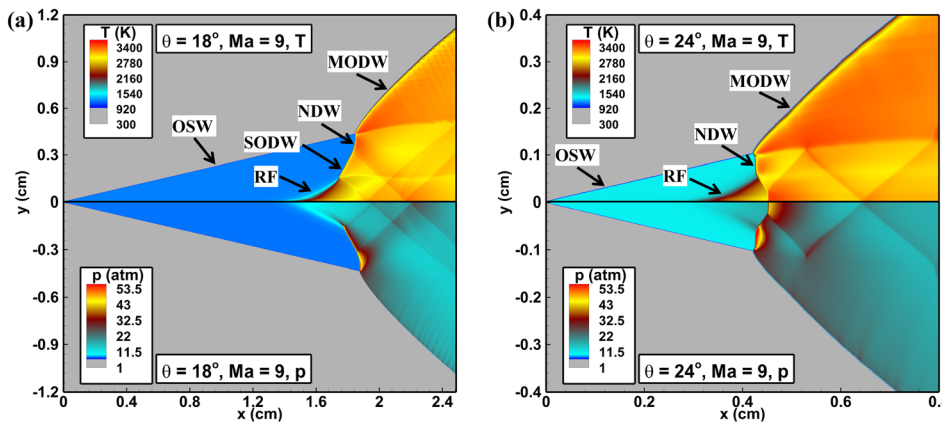


**FIG. 3.** Temperature (upper) and pressure (lower) contours with wedge angle of (a)  $\theta = 18^\circ$  and (b)  $\theta = 24^\circ$ .

that the abrupt transition of OSW–ODW occurs at  $\theta = 18^\circ$ . The ODW structure consists of a reaction front (RF), a secondary oblique detonation wave (SODW), a normal detonation wave (NDW), and the main oblique detonation wave (MODW). The post-OSW flow state is  $V = 2126.8$  m/s,  $T = 1242.8$  K, and  $P = 7.67$  atm, respectively, at which the corresponding homogeneous ignition delay time is  $\tau_{ig} = 7.18 \mu\text{s}$ . The theoretical ignition length, that is, the product of homogeneous ignition delay time and flow velocity behind the OSW, is  $L_i = 1.53$  cm, and it is very close to the ignition length of  $L_i = 1.47$  cm predicted by 2D simulation. As  $\theta$  increases to  $24^\circ$ , the MODW and RF are directly connected by the NDW, see Fig. 3(b), while it still belongs to the abrupt transition. The theoretical ignition length is  $0.314$  cm, which is also close to the ignition length of  $L_i = 0.32$  cm predicted by 2D simulation. The steady ODW structures shown in Fig. 3 are used as references for the subsequent transient simulations.

Before evaluating the effects of wedge-angle change on ODW structure evolutions, we need verify the difference between IAC and WAC. The ODW structure evolutions in attack-angle increasing process for IAC and WAC are compared in the Appendix and sketched in Fig. 4. The influence regime of WAC is sketched in Fig. 4(a), which is obviously different from previous studies.<sup>22,24</sup> For WAC, the disturbance caused by moving wedge [denoted by blue dashed lines in Fig. 4(a)] propagates along the Mach angle. As the disturbance reaches to the OSW, it leads to considerable increase in temperature and pressure of the mixtures behind the OSW, and accordingly, the ODW is enhanced. The ODW around wedge surface is first affected, and then, the pressure waves propagate from the wedge surface to the OSW. However, the influence regime of IAC is different from WAC. As shown in Fig. 4(b), the disturbance propagates downstream from the inlet boundary, and the fluid near the OSW is influenced at first and

the newly formed OSW expands downstream from the leading edge. Therefore, the original main ODW structure is not immediately affected by IAC until the disturbance reaches its location. The compression waves induced by WAC propagate upward from the wedge surface while that caused by IAC propagate downward along the wedge surface, respectively. In general, the flow configurations of IAC are not equivalent to those of WAC, and consequently, the transient evolution of ODW caused by IAC would be utterly different from that due to WAC (see the Appendix).

### B. Wave structure evolutions during wedge-angle change process

In this section, we examined the oblique detonation wave structure evolution and the influence of wedge-rotation angular velocity for the WAC process met in practical application. For the WAC process, the wedge angle is assumed to range between  $24^\circ$  and  $18^\circ$ . The duration time of angle change is represented by  $T_c$ .

The ODW evolutions induced by the wedge angle that increases from  $18^\circ$  to  $24^\circ$  within  $5 \mu\text{s}$  are simulated, yielding the temperature contours shown in Fig. 5. The initial ODW configuration ( $t = 0 \mu\text{s}$ ) is shown in Fig. 3(a). Due to the wedge compression, the reaction front moves upstream and the ignition length reduces from  $1.47$  to  $0.97$  cm at  $t = 2 \mu\text{s}$ . As the wedge angle reaches  $\theta = 24^\circ$  at  $t = 5 \mu\text{s}$ , the reaction front further moves upstream and the ignition length reduces to  $L_i = 0.42$  cm, which is still larger than the steady value of  $L_i = 0.32$  cm for  $\theta = 24^\circ$ . It exhibits lag of the ignition length evolution to the wedge rotation. The ignition point near the wedge surface continuously moves upstream until  $t = 7.5 \mu\text{s}$ , whereas the downstream ODW surface needs more time to satisfy the wedge variation for the hysteretic nature of disturbance.

The reverse process of decreasing the wedge angle from  $24^\circ$  to  $18^\circ$  is subsequently simulated, and the results are shown in Fig. 6. The transient ODW structure evolution can be roughly divided into three stages. During the first stage with the wedge angle changing from  $24^\circ$  to  $21.6^\circ$  [see Figs. 6(a) and 6(b)], the ignition point and the reaction front move downstream due to the expansion wave induced by angle decreasing. It reduces the temperature and pressure behind the OSW and thereby delays the autoignition of local reactants. There is no obvious movement of the triple point during the first stage of  $0 \leq t \leq 5 \mu\text{s}$ . Moreover, the reaction front near the wedge surface moves rapidly

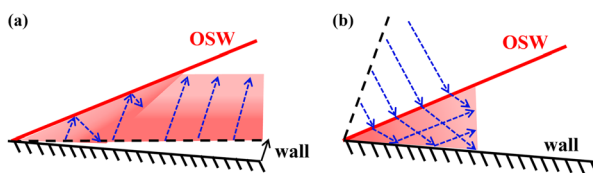


**FIG. 4.** The influence regimes of the disturbance during the angle increasing process for (a) WAC and (b) IAC.

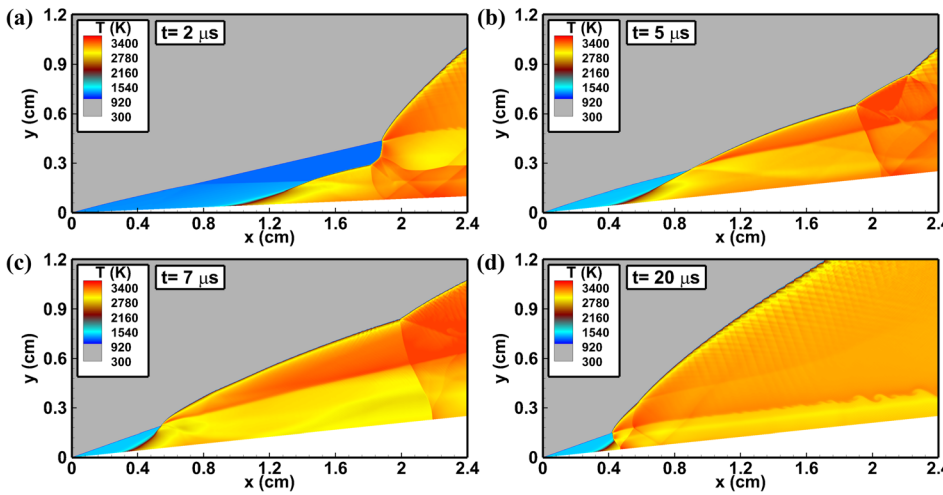


**FIG. 5.** Evolution of temperature contour for WAC ( $18^\circ$  to  $24^\circ$ ) with  $T_c = 5 \mu\text{s}$ : (a)  $t = 2$ ; (b)  $t = 5$ ; (c)  $t = 7$ ; and (d)  $t = 20 \mu\text{s}$ . The structure at  $t = 0 \mu\text{s}$  has been shown in Fig. 3(a).

downstream and merges with the NDW at  $t = 5 \mu\text{s}$ , forming a triple-wave structure consisting of OSW, NDW, and MODW, as shown in Fig. 6(c). In the second stage with  $5 \leq t \leq 48 \mu\text{s}$ , the triple-wave structure moves downstream [see Figs. 6(c) and 6(d)], which lasts much longer than the first stage. The NDW moves downstream since its CJ speed is lower than the post OSW flow speed. Finally, in the third stage, autoignition appears on the wedge surface producing reaction front subsequently, which can be attributed to that the distance between the NDW and the wedge tip is larger than the theoretical ignition length. Finally, the steady ODW structure shown in Fig. 3(a) is gradually recovered [see Figs. 6(e) and 6(f)].

As shown in Fig. 5, the WAC from  $18^\circ$  and  $24^\circ$  induces continuous movement of the reaction front toward the leading edge. This

evolution process depends upon the mixture's reactivity, which suggests that the chemical kinetics plays a crucial role in determining the newly formed ODW fields. In the meanwhile, Fig. 6 shows that the unsteady process induced by WAC from  $24^\circ$  to  $18^\circ$  is characterized by the downstream movement of the NDW, which is dominated by shock wave dynamics. This evolution process seriously lags behind the wedge rotation.

For the above-mentioned cases, we fix the duration of angle-change time to  $T_c = 5 \mu\text{s}$ . Then, the influence of wedge-rotation angular velocity for WAC is evaluated. Here, we consider WAC at different values of  $T_c$ , that is, different wedge-rotation angular velocities. Figure 7 shows the evolution of the ignition length along the wedge surface for different values of  $T_c = 1, 3, 5$ , and  $10 \mu\text{s}$ . As the rotational

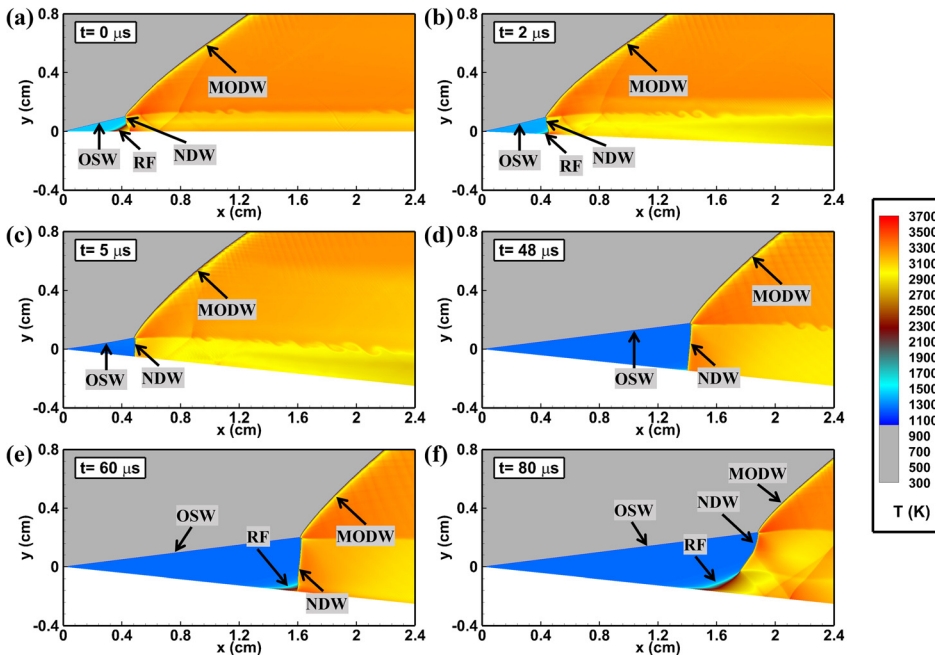


**FIG. 6.** Temporal evolution of temperature contour for WAC from  $24^\circ$  to  $18^\circ$  within  $T_c = 5 \mu\text{s}$ : (a)  $t = 0$ ; (b)  $t = 2$ ; (c)  $t = 5$ ; (d)  $t = 48$ ; (e)  $t = 60$ ; and (f)  $t = 80 \mu\text{s}$ .

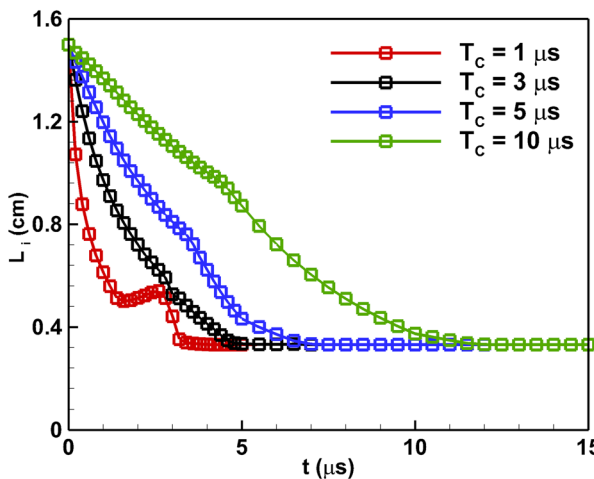


**FIG. 7.** Change of the ignition length,  $L_i$ , varies with time for WAC from  $18^\circ$  to  $24^\circ$  and different values of  $T_c$ .

angular velocity of the wedge decreases, the recovery times of ODW fields are 4.4, 5.5, 7.5, and 12.0  $\mu\text{s}$ , respectively. In all cases, the induction times to establish the new steady states are within about 4  $\mu\text{s}$  when the wedge rotation stops. For  $T_c = 1 \mu\text{s}$  (marked by the red curve in Fig. 7), the ignition length changes non-monotonically with time. To interpret the non-monotonic phenomenon, we conduct particle tracking analysis. The trajectories of four tracked fluid particles are shown in Fig. 8(a). The evolutions of the temperatures, pressures, and local ignition delay times for these four particles are presented in Figs. 8(b)–8(d).

For particle No. 1 in Fig. 8, its temperature decreases from 1492 to 1301 K and pressure decreases from 15.1 to 10.9 atm at about  $t = 1 \mu\text{s}$ . Consequently, its ignition delay time increases from 0.6 to 1  $\mu\text{s}$ , which leads to the extension of ignition length shown in Fig. 7. The wedge stops rotating at  $t = T_c = 1 \mu\text{s}$ , while the fluid particle continues to move away from the wedge surface due to its inertia. This induces the decrease in the temperature and pressure experienced by the tracked particle and thus explains the non-monotonic change in temperature and pressure presented in Figs. 8(b) and 8(c). Furthermore, the fall of pressure and temperature lowers the local reaction rate and thereby prolongs the total ignition time, that is, ignition length because of nearly constant flow velocity behind the OSW. For the particles Nos. 2, 3, and 4, their temperature and pressure also decrease at around  $t = 1.4$ , 1.7, and 2.1  $\mu\text{s}$ , respectively, which can be attributed to the same dominating mechanism. For large  $T_c$ , the angular velocity of wedge rotation is slow and thereby the fluid inertia effect tends to be weak. Moreover, a newly formed OSW could appear during the wedge rotation process, according to which the reactant states near wedge surface can be determined. These two factors result in a monotonous change of the ignition length for  $T_c = 3$ , 5, and 10  $\mu\text{s}$ . Therefore, the non-monotonic trend is only observed in Fig. 7 for  $T_c = 1 \mu\text{s}$ .

We also consider the WAC from  $24^\circ$  to  $18^\circ$  at different angular velocities. The influence of  $T_c$  on ignition length is assessed by monitoring the variation of ignition length in the course of time [see Fig. 9(a)]. It indicates that the evolution of ignition length tends to be independent of  $T_c$  in each individual stage introduced in the preceding

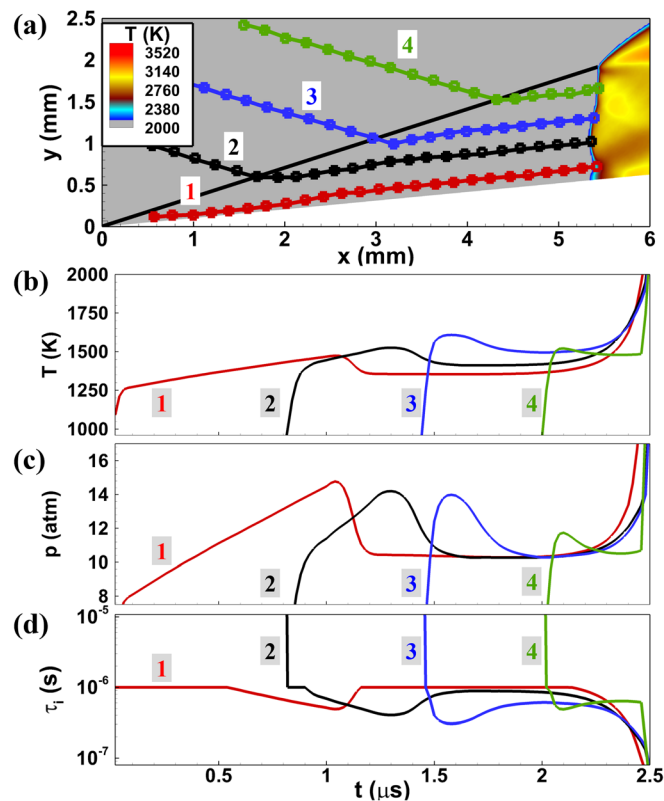


**FIG. 8.** Path tracking analysis for the evolution of four particles during WAC from  $18^\circ$  to  $24^\circ$  within  $T_c = 1 \mu\text{s}$ : (a) particles trajectories, (b) temperature, (c) pressure, and (d) the corresponding ignition delay time.

discussion. Therefore, the angular velocity of wedge rotation exhibits little influence on transient evolution of the ODW structure during the process of wedge-angle reduction. Moreover, the presented curves almost have the same slope in the second stage for different wedge-rotation angular velocities in Fig. 9(b), which implies that the propagation of NDW in the second stage would be independent of the wedge-rotation angular velocity. The propagation velocity of the NDW relative to the inflow, shown in Fig. 9(b), is very close to the theoretical C-J speed.

### C. Polar curve analysis for wave structure

An interesting phenomenon in Fig. 9 is that the movement speed of the NDW on the wedge surface almost remains to be constant. We further calculate the density schlieren of the wave structure for  $T_c = 5 \mu\text{s}$ . The diagrams (black lines) at different times ( $t = 10, 20, 30$ , and  $40 \mu\text{s}$ ) are shown in Fig. 10(a). In the red dashed box, the wave structure is nearly self-similar and almost remains the same at different times. The pressure distributions along the blue line (parallel to OSW and the distance between blue line and OSW is about 0.5 mm) are extracted. The jumping position of pressure is shifted to the same point, and the pressure profiles are plotted in Fig. 10(b). It is seen that the pressure distributions among the flow fields at different times are almost the same. Such comparison demonstrates that the triple-wave

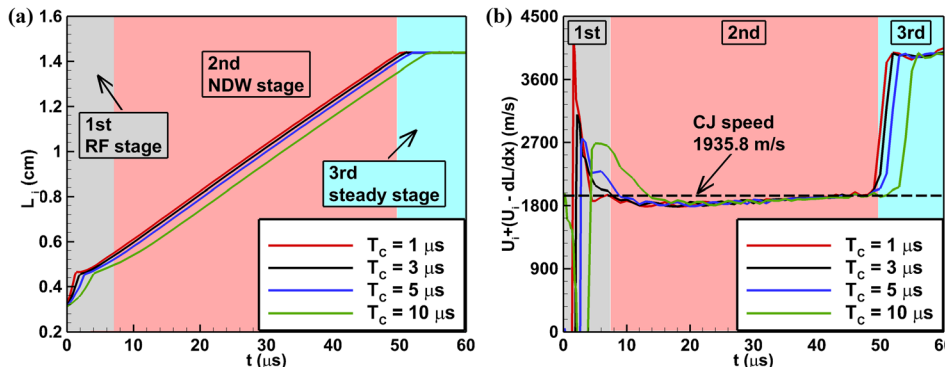


**FIG. 9.** (a) The ignition length,  $L_i$ , and (b) the velocity of the NDW relative to the flow before the NDW,  $U + (U_r dL/dx)$  for WAC from  $24^\circ$  to  $18^\circ$  and different values of  $T_c$ .

structure in the second stage of the wedge-angle decreasing process is quasi-steady. Therefore, the polar curve can be used to analyze the wave structure.

As mentioned before, the shock wave dynamics plays the main role during wedge-angle decreasing process and an important feature is the quasi-steady triple-wave structure. To explain the formation of the triple-wave structure in Fig. 10, the local flow structure at  $t = 48 \mu\text{s}$  is enlarged and its pressure, density, and schlieren contours are described in Figs. 11(a)–11(c). In Figs. 11(a) and 11(b), there exists a reflect shock wave (RSW) that connects the NDW, OSW, and MODW. The presence of RSW is to satisfy the gas pressure behind NDW and MODW. The schlieren contour is calculated via the second-order gradient of density, and the white streamlines are also given in Fig. 11(c). The schematic of the corresponding multi-wave system is plotted in Fig. 11(d) to clearly display the wave structures. Note that the symbol  $\beta$  denotes the angle between the wave and the pre-wave streamline, and  $\theta$  corresponds to the deflection angle of flow behind the wave relative to the pre-wave flow. The simulated inflow deflection angle across the OSW,  $\theta_{1-2,S}$ , equals to  $18^\circ$ , while the angle,  $\beta_{1-2,S}$ , between the inflow and the OSW equals to  $31^\circ$ . The inflow deflection angle across the RSW,  $\theta_{2-3,S}$ , is  $19^\circ$ , while the gas-stream deflection angle across the RSW,  $\beta_{2-3,S}$ , equals to  $48^\circ$ .

To analyze the formation of wave structure in the initiation zone, the typical polar curve is employed here. For the stoichiometric hydrogen/air mixture with a detailed reaction model, it is virtually impossible to accurately represent the relationship between detonation product and unburned mixture via a simplified formula. The thermodynamic properties and chemical compositions strongly depend on the local temperature and pressure. Therefore, an iteration approach is required to solve shock jumping relations coupled with the chemical

equilibrium. Using the open-source software SD Toolbox (Shock and Detonation Toolbox),<sup>41</sup> the product pressure/temperature at equilibrium state and the oblique wave angle can be obtained. Similar methods were used in various scenarios<sup>42</sup> showing the predictability of polar curve theory in shock/detonation wave dynamics.

The  $P$ – $\theta$  polar [denoting the gas state of region No. 1 in Fig. 11(d)] is first calculated and plotted in Fig. 12, in which the shock and detonation polar curves are marked by blue and red lines. The black line is used to display the shock polar of region No. 2. From Fig. 12, the intersection point of black line and red line is located at the strong branch of detonation polar, implying that the local MODW is a strong detonation solution. In region No. 2, the flow has been compressed by OSW and its theoretical Mach number decreases to 2.54 for the increasing temperature and decreasing mixtures velocity. When the compressed mixtures across the RSW from region No. 2 to 3. The pressure behind MODW should equal to that behind the RSW. Through the polar theory in Fig. 12, the thermodynamic state in region No. 2 can be calculated easily ( $P = 7.96 \text{ atm}$ ,  $T = 1308.0 \text{ K}$ ,  $V = 2114.4 \text{ m/s}$ ). The intersection point of these two pressure polar curves (separately for the MODW and for the RSW) corresponds to the theoretical pressure ( $P_{3,T} = P_{4,T} = 26.9 \text{ atm}$ ) in region Nos. 3 and 4.

The  $\beta$ – $\theta$  polar curves for shock/detonation waves are plotted in Fig. 13, in which the angle  $\beta$  is defined as the included angle between local flow and shock wave front. For the wedge angle  $\theta_{1-2} = 18^\circ$ , the theoretical inflow–OSW angle  $\beta_{1-2,T}$  is  $31.9^\circ$  that is consistent with the numerical results in Fig. 11. The semi-infinite wedge-induced ODW angle  $\beta_{1-5,T}$  is  $53.1^\circ$  that is far lower than the angle of strong detonation predicted by polar theory. Across the RSW, the inflow deflection angle,  $\theta_{2-3,T}$ , equals to  $21.5^\circ$  and the theoretical angle  $\beta_{2-3,T}$  between the local flow and the RSW is  $44.3^\circ$  (Fig. 13). Overall, the shock wave

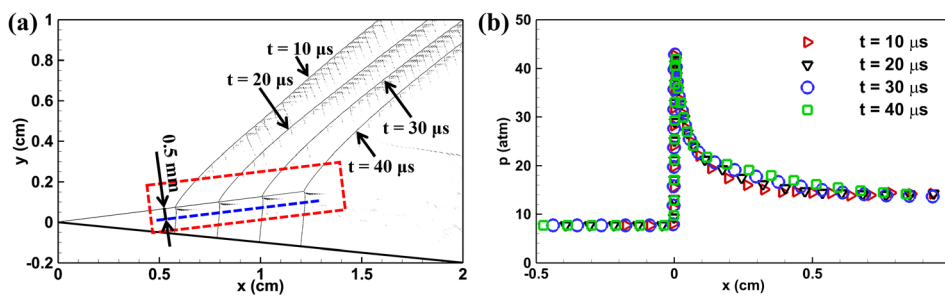


**FIG. 10.** (a) The density schlieren diagrams of the wave structures at different times. (b) The pressure distributions shifted to the same peak pressure position along the blue line in (a).

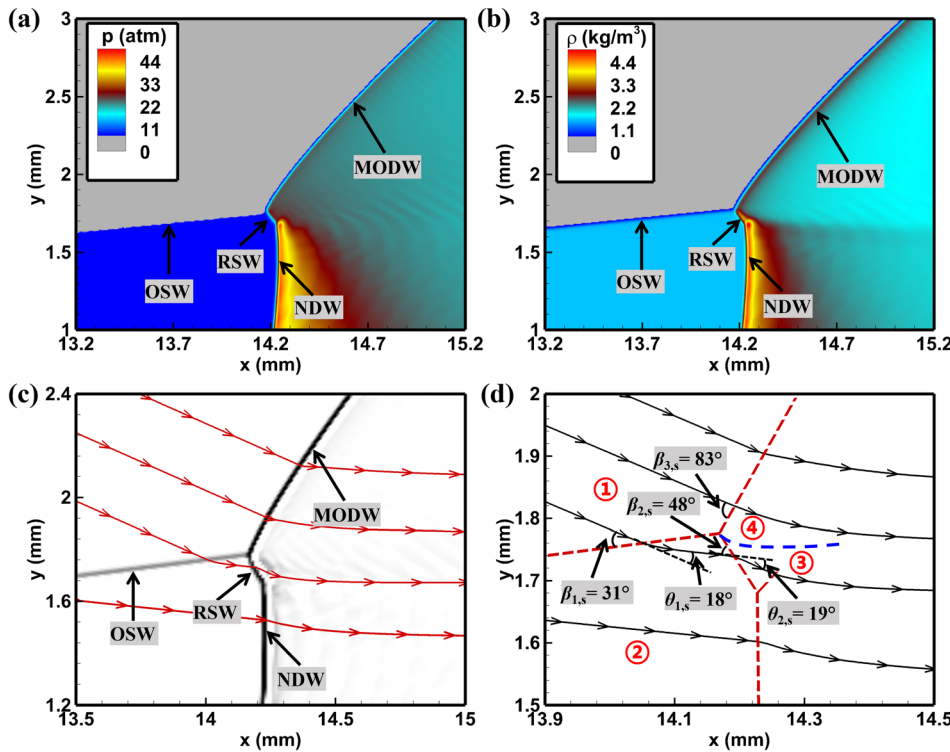


**FIG. 11.** The partial structure of (a) pressure, (b) density, (c) schlieren contours, and (d) wave system structure at  $t = 48 \mu\text{s}$  for WAC from  $24^\circ$  to  $18^\circ$  with  $T_c = 5 \mu\text{s}$ .

polar curve (black line in Fig. 12) intersects with the strong branch of detonation wave polar curve (red line in Fig. 12), which means the local MODW near the initiation zone is a strong solution whose pressure is far larger than the semi-infinite wedge-induced ODW. Hence, a strong reflected shock wave must form to satisfy the high pressure behind the MODW. The newly reflected shock wave interacts with the

bottom wedge and different reflection patterns can be probability observed in the WAC process.

The above analysis is helpful for understanding the formed RSW and MODW, and the other key issue to be resolved is the formation mechanism of NDW on the wedge surface. The wave structure predicted by the theoretical polar curve analysis is described in Fig. 14(a).

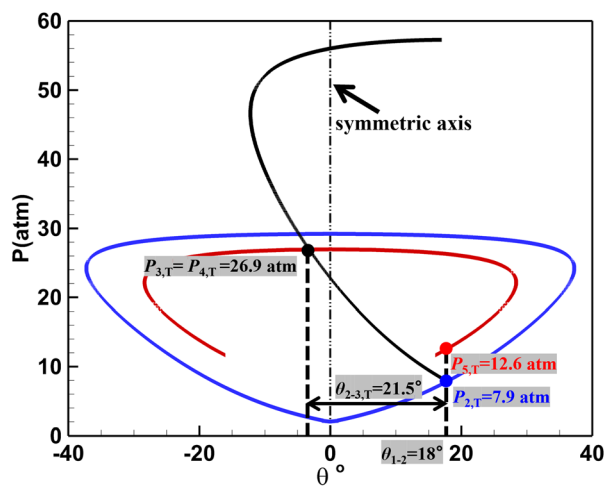


**FIG. 12.** The  $P-\theta$  polar curves for oblique shock wave (blue line) and detonation wave (red line) with  $Ma = 3.59$  and for oblique shock wave for  $Ma = 2.54$  (black line).

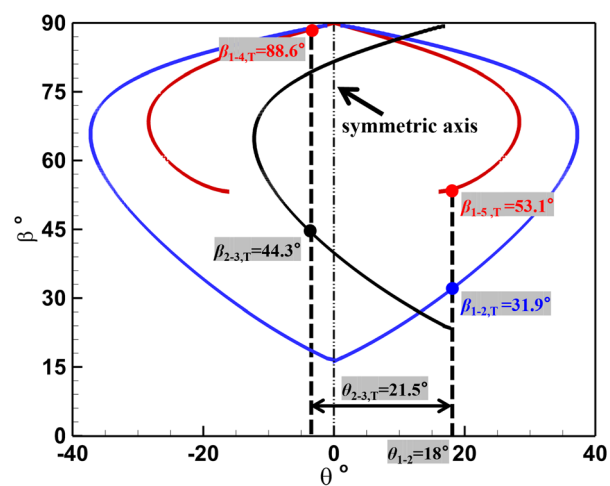


**FIG. 13.** The  $\beta-\theta$  polar curves for oblique shock wave (blue line) and detonation wave (red line) with  $Ma = 3.59$  and for oblique shock wave for  $Ma = 2.54$  (black line).

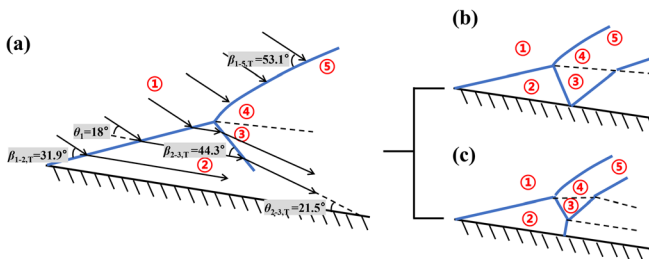


**FIG. 14.** (a) The wave system structure predicted by the polar curve theory and two possible more specific structures: (b) regular reflection and (c) Mach reflection structure.

It is in good agreement with the simulated wave structures in Fig. 11(d). The shock wave between region Nos. 3 and 2 will interact with the wedge, and two possible structures, regular reflection [seen in Fig. 14(b)] and Mach reflection [seen in Fig. 14(c)], may occur. The interaction pattern between the RSW and the wedge mainly depends on the inflow state in region No. 2 and the RSW angle. In general, the large wave angle promotes the presence of Mach stem in Fig. 14(c).

Then, the formation of the NDW in angle-decreasing process is clarified. In Fig. 15,  $\theta_D$  is the critical angle given by detachment condition and  $\theta_N$  is the critical angle given by von Neumann condition.<sup>43</sup> If the inflow deflection angle  $\theta_{2-3} < \theta_N$ , then the regular reflection will occur; while if the inflow deflection angle  $\theta_{2-3} > \theta_D$ , then the Mach reflection will occur. Double solution may exist if  $\theta_N < \theta_{2-3} < \theta_D$ . According to the theoretical inflow state analysis in region No. 2 in Fig. 14(a),  $\theta_{2-3,T}=21.5^\circ$  and the Mach number equals to 2.54. From Fig. 15, the corresponding angle is to be located above  $\theta_N$  curve. That means the Mach reflection in Fig. 14(c) will happen for the RSW between region Nos. 2 and 3, which is consistent with the numerical result in Fig. 11(d).

#### IV. CONCLUSIONS

Two-dimensional simulations with detailed chemistry are conducted for wedge-induced oblique detonation wave in a stoichiometric

hydrogen/air mixture. Practical thermodynamic states are considered for the inflow based on the flight altitude and Mach number. The transient evolutions of ODW structure caused by inflow-angle change (IAC) and wedge-angle change (WAC) are examined. It is found that the compression waves induced by WAC and IAC propagate upward from the wedge surface and downward along the wedge surface, respectively. It demonstrates that the flow configuration corresponding to WAC and IAC is not equivalent. The ODW structure evolution during the WAC process in practical application is discussed in-depth via numerical simulated, adopting dynamic mesh to reproduce the rotation of wedge surface during WAC. During the wedge angle increasing process, the reaction front (thermodynamic properties of mixtures) is dominant for ODW structure evolution. Nevertheless, the shock wave (dynamic properties) appears in the reverse process and is dominant for ODW structure evolution. In addition, the effects of angular velocity of wedge rotation on transient ODW structure evolution are assessed. It is found that the evolution of the ODW structure is more sensitive to the angular velocity of wedge rotation for increasing wedge angle than for decreasing wedge angle. Considering the quasi-steady characteristic during the wedge angle decreasing process, the polar curve analysis is conducted. The wave structures predicted by theory are consistent with those recorded in the numerical simulations. In future works, it would be interesting to take viscosity into account and investigate the influence of the boundary layer on the evolution of detonation structure during WAC and IAC.

#### SUPPLEMENTARY MATERIAL

See the [supplementary material](#) for the complete code validation in which the solver (detonationFoam) based on OpenFOAM is examined.

#### ACKNOWLEDGMENTS

This work was supported by the National Natural Science Foundation of China (Nos. 52176096, 52006001, and 12202014), China Postdoctoral Science Foundation (No. 2021M700222), and Open Project of the State Key Laboratory of High Temperature Gas Dynamics (No. 2021KF01). We thank Dr. Dehai Yu from Peking University for his linguistic assistance during the preparation of this manuscript.

#### AUTHOR DECLARATIONS

##### Conflict of Interest

The authors have no conflicts to disclose.

##### Author Contributions

**Jie Sun:** Formal analysis (lead); Methodology (lead); Software (lead); Writing – original draft (lead). **Pengfei Yang:** Conceptualization (lead); Formal analysis (lead); Investigation (equal); Writing – review & editing (equal). **Baolin Tian:** Formal analysis (supporting); Supervision (supporting); Writing – review & editing (supporting). **Zheng Chen:** Investigation (supporting); Supervision (equal); Validation (supporting); Writing – review & editing (supporting).

#### DATA AVAILABILITY

The data that support the findings of this study are available from the corresponding author upon reasonable request.

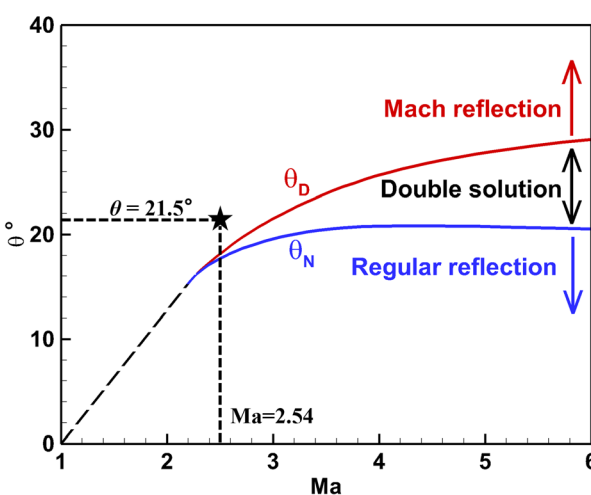


**FIG. 15.** The  $\theta$ - $Ma$  curves predicted by detachment criterion (red line) and von Neumann criterion (blue line).

## APPENDIX: EFFECTS OF INFLOW ANGLE CHANGE ON ODW EVOLUTIONS

In Sec. III B, we consider WAC from  $18^\circ$  to  $24^\circ$  within  $T_c = 5 \mu\text{s}$ . Here, we consider IAC from  $18^\circ$  to  $24^\circ$  within  $T_c = 5 \mu\text{s}$ , for which the results are shown in Fig. 16, to compare the results with that for WAC in Fig. 5. Though the inflow angle has changed to  $24^\circ$  at  $t = 5 \mu\text{s}$  in Fig. 16(a), the ODW structure is almost the same as the initial steady structure at  $\theta = 18^\circ$  shown in Fig. 3(a). Unlike the WAC process shown in Fig. 5, Fig. 16(b) shows that a new ignition point and new reaction front appear before the original reaction front. The ignition length corresponding to this new reaction front is around  $L_i = 0.38 \text{ cm}$ , which is slightly larger than the steady ignition length of  $L_i = 0.32 \text{ cm}$  for  $\theta = 24^\circ$ . Subsequently, Fig. 16(c) shows that the new reaction front expands outwardly, forming a new main ODW between the OSW and the original main ODW. Finally, the steady ODW structure forms at around  $t = 20 \mu\text{s}$  as shown in Fig. 16(d).

Though the final steady ODW structures shown in Figs. 5(d) and 16(d), respectively, for WAC and IAC are same, their evolution is obviously different. Specifically, the development of the new main ODW between the OSW and the original main ODW is completely different during WAC (Fig. 5) and IAC (Fig. 16). For the WAC process, the original reaction front successively expands upstream. However, a new reaction front appears before the original one during the IAC process. Note that the appearance of the new reaction front before the original one was also observed by Zhang *et al.*<sup>24</sup> The results in Figs. 5 and 16 indicate that WAC and IAC are not equivalent. Therefore, simply modifying inflow direction at the inlet boundary cannot model the ODW control through changing the wedge angle for fixed inflow.

To further interpret the influence of WAC and IAC on ODW structure evolution, we compare the detailed evolutions of pressure contour near the leading edge for WAC and IAC in Fig. 17.

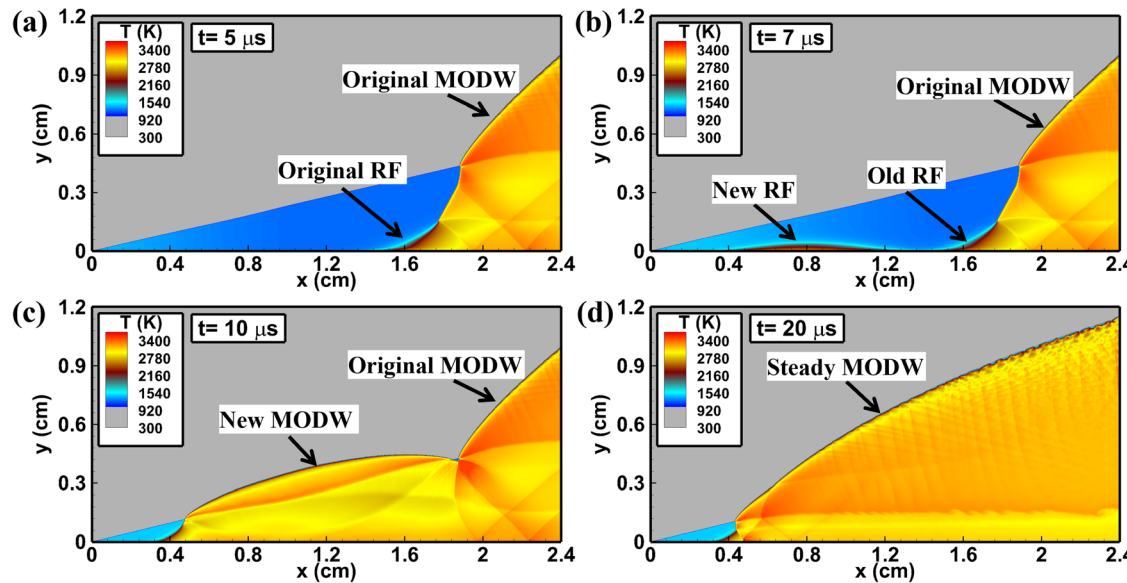


FIG. 16. Temporal evolution of temperature contour for IAC from  $18^\circ$  to  $24^\circ$  within  $T_c = 5 \mu\text{s}$ : (a)  $t = 5$ ; (b)  $t = 7$ ; (c)  $t = 10$ ; and (d)  $t = 20 \mu\text{s}$ . The result for  $t = 0 \mu\text{s}$  has been shown in Fig. 3(a).

For WAC at  $t = 0 \mu\text{s}$ , the reaction front and ODW structure are outside the region shown in Fig. 17(a). At  $t = 1 \mu\text{s}$ , the wedge angle is increased from  $18^\circ$  to  $19.2^\circ$ , and the pressure and temperature on the wedge surface both increase since the fluid is squeezed and compressed by the moving wall/wedge. Since the pressure and temperature increase reduces the ignition delay time, the ignition point moves toward the leading edge and reaches  $x = 1.12 \text{ cm}$  at  $t = 1 \mu\text{s}$ . As shown in Figs. 17(b) and 17(c), the pressure wave/disturbance propagates from line A at  $t = 1 \mu\text{s}$  to line B at  $t = 2 \mu\text{s}$ , and the reaction front further moves toward the leading edge due to the continuous compression caused by wedge rotation. When the pressure wave interacts with the OSW, the OSW evolves into a new state following the  $\theta$ - $\beta$ - $Ma$  law.<sup>44,45</sup> The main ODW does not form simultaneously during WAC since the disturbance needs to travel a certain distance before its interaction with the OSW. Consequently, the reaction front at  $t = 5 \mu\text{s}$  shown in Fig. 17(d) still does not reach the steady state. Therefore, wedge compression induces the reaction front to move upstream, as shown in Figs. 17(a)-17(d).

However, for the IAC process shown in Figs. 17(e)-17(h), as the time increases from  $t = 0$  to  $t = 4 \mu\text{s}$ , the pressure near the leading edge increases first. The influence of IAC propagates downwardly. As shown in Figs. 17(f) and 17(g), the pressure wave/disturbance propagates from line A' at  $t = 4 \mu\text{s}$  to line B' at  $t = 6 \mu\text{s}$ . At  $t = 7 \mu\text{s}$ , new ignition happens around  $x = 0.3 \text{ cm}$  and new reaction front [represented by the dashed lines in Fig. 17(h)] develops.

Figure 17 shows that the mixture far from the leading edge is first compressed for WAC, while the opposite holds for IAC. Therefore, as shown in Figs. 5, 16, and 17, the ignition point continuously moves upward for WAC while new ignition point develops for IAC. This is the main difference in the ODW structure evolutions induced by WAC and IAC. The influence regimes for IAC and WAC are concluded and sketched in Fig. 4.

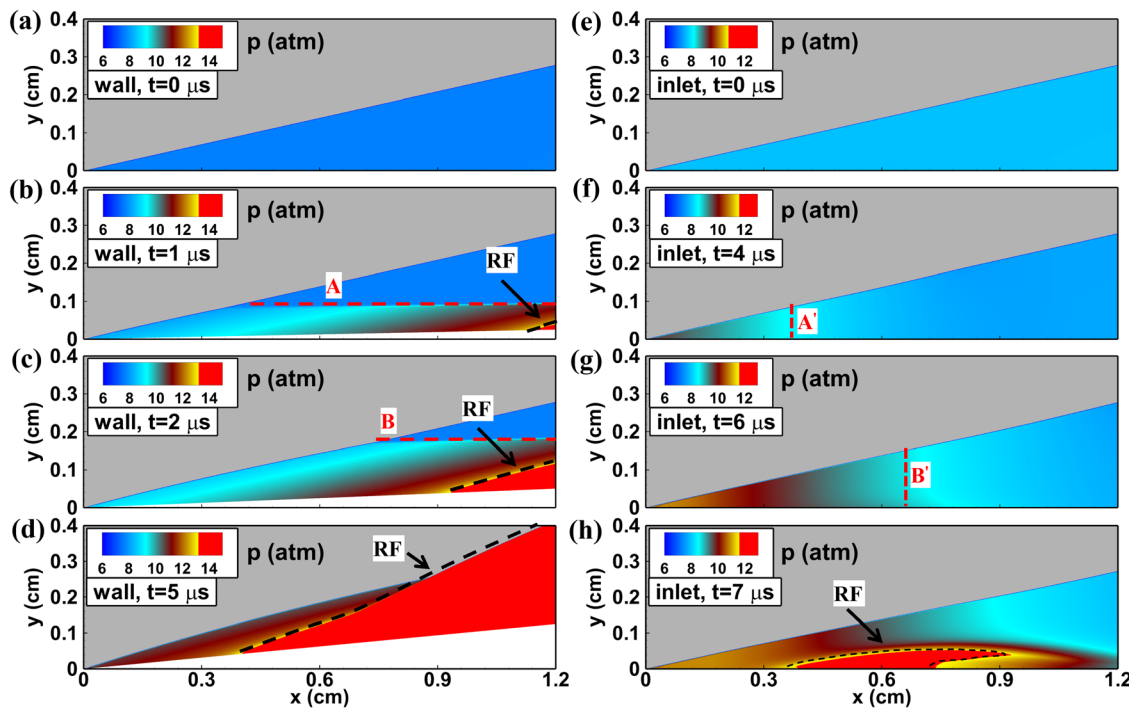


FIG. 17. Temporal evolution of local pressure contour near the leading edge for WAC [figures (a)–(d)] and IAC [figures (e)–(h)] from  $18^\circ$  to  $24^\circ$  within  $T_c = 5 \mu\text{s}$ .

## REFERENCES

- <sup>1</sup>P. Wolański, “Detonative propulsion,” *Proc. Combust. Inst.* **34**, 125–158 (2013).
- <sup>2</sup>B. A. Rankin, M. L. Fotia, A. G. Naples, C. A. Stevens, J. L. Hoke, T. A. Kaemming, S. W. Theuerkauf, and F. R. Schauer, “Overview of performance, application, and analysis of rotating detonation engine technologies,” *J. Propul. Power* **33**, 131–143 (2017).
- <sup>3</sup>G. D. Roy, S. M. Frolov, A. A. Borisov, and D. W. Netzer, “Pulse detonation propulsion: Challenges, current status, and future perspective,” *Prog. Energy Combust. Sci.* **30**, 545–672 (2004).
- <sup>4</sup>X. Qie, Z. Ji, H. Wen, Z. Ren, P. Wolanski, and B. Wang, “Review on the rotating detonation engine and its typical problems,” *Trans. Aerosp. Res.* **2020**, 107–163 (2020).
- <sup>5</sup>R. Zhou, D. Wu, and J. Wang, “Progress of continuously rotating detonation engines,” *Chin. J. Aeronaut.* **29**, 15–29 (2016).
- <sup>6</sup>S. Elhawary, A. Saat, M. A. Wahid, and A. D. Ghazali, “Experimental study of using biogas in pulse detonation engine with hydrogen enrichment,” *Int. J. Hydrogen Energy* **45**, 15414–15424 (2020).
- <sup>7</sup>D. Schwer and K. Kailasanath, “Numerical investigation of the physics of rotating-detonation-engines,” *Proc. Combust. Inst.* **33**, 2195–2202 (2011).
- <sup>8</sup>Z. Zhang, C. Wen, W. Zhang, Y. Liu, and Z. Jiang, “Formation of stabilized oblique detonation waves in a combustor,” *Combust. Flame* **223**, 423–436 (2021).
- <sup>9</sup>C. Li, K. Kailasanath, and E. S. Oran, “Detonation structures behind oblique shocks,” *Phys. Fluids* **6**, 1600–1611 (1994).
- <sup>10</sup>Y. Liu, Y. S. Liu, D. Wu, and J. P. Wang, “Structure of an oblique detonation wave induced by a wedge,” *Shock Waves* **26**, 161–168 (2016).
- <sup>11</sup>A.-F. Wang, W. Zhao, and Z.-L. Jiang, “The criterion of the existence or inexistence of transverse shock wave at wedge supported oblique detonation wave,” *Acta Mech. Sin.* **27**, 611–619 (2011).
- <sup>12</sup>J. Verreault and A. J. Higgins, “Initiation of detonation by conical projectiles,” *Proc. Combust. Inst.* **33**, 2311–2318 (2011).
- <sup>13</sup>H. Teng, C. Tian, Y. Zhang, L. Zhou, and H. D. Ng, “Morphology of oblique detonation waves in a stoichiometric hydrogen-air mixture,” *J. Fluid Mech.* **913**, A1 (2021).
- <sup>14</sup>M. V. Papalexandris, “A numerical study of wedge-induced detonations,” *Combust. Flame* **120**, 526–538 (2000).
- <sup>15</sup>Y. Liu, D. Wu, S. Yao, and J. Wang, “Analytical and numerical investigations of wedge-Induced oblique detonation waves at low inflow Mach number,” *Combust. Sci. Technol.* **187**, 843–856 (2015).
- <sup>16</sup>Y. Fang, Y. Zhang, X. Deng, and H. Teng, “Structure of wedge-induced oblique detonation in acetylene-oxygen-argon mixtures,” *Phys. Fluids* **31**, 026108 (2019).
- <sup>17</sup>M. Yu and S. Miao, “Initiation characteristics of wedge-induced oblique detonation waves in turbulence flows,” *Acta Astronaut.* **147**, 195–204 (2018).
- <sup>18</sup>L. F. Figueira Da Silva and B. Deshaies, “Stabilization of an oblique detonation wave by a wedge: A parametric numerical study,” *Combust. Flame* **121**, 152–166 (2000).
- <sup>19</sup>K. Iwata, S. Nakaya, and M. Tsue, “Wedge-stabilized oblique detonation in an inhomogeneous hydrogen-air mixture,” *Proc. Combust. Inst.* **36**, 2761–2769 (2017).
- <sup>20</sup>Y. Fang, Z. Hu, H. Teng, Z. Jiang, and H. D. Ng, “Numerical study of inflow equivalence ratio inhomogeneity on oblique detonation formation in hydrogen-air mixtures,” *Aerosp. Sci. Technol.* **71**, 256–263 (2017).
- <sup>21</sup>H. Teng, H. D. Ng, and Z. Jiang, “Initiation characteristics of wedge-induced oblique detonation waves in a stoichiometric hydrogen-air mixture,” *Proc. Combust. Inst.* **36**, 2735–2742 (2017).
- <sup>22</sup>Y. Liu, L. Wang, B. Xiao, Z. Yan, and C. Wang, “Hysteresis phenomenon of the oblique detonation wave,” *Combust. Flame* **192**, 170–179 (2018).
- <sup>23</sup>P. Yang, H. D. Ng, and H. Teng, “Unsteady dynamics of wedge-induced oblique detonations under periodic inflows,” *Phys. Fluids* **33**, 016107 (2021).
- <sup>24</sup>Y. Zhang, P. Yang, H. Teng, H. D. Ng, and C. Wen, “Transition between different initiation structures of wedge-induced oblique detonations,” *AIAA J.* **56**, 4016–4023 (2018).

- <sup>25</sup>OpenFOAM V6, see <https://openfoam.org> for the introduction and the user guide for OpenFOAM V6.
- <sup>26</sup>H. Jasak, "Dynamic mesh handling in OpenFOAM," in The 47th AIAA Aerospace Sciences Meeting Including the New Horizons Forum and Aerospace Exposition, 2009.
- <sup>27</sup>M. P. Burke, M. Chaos, Y. Ju, F. L. Dryer, and S. J. Klippenstein, "Comprehensive H<sub>2</sub>/O<sub>2</sub> kinetic model for high-pressure combustion," *Int. J. Chem. Kinetics* **44**, 444–474 (2012).
- <sup>28</sup>Q. Li, E. Hu, X. Zhang, Y. Cheng, and Z. Huang, "Laminar flame speeds and flame instabilities of pentanol isomer-air mixtures at elevated temperatures and pressures," *Energy Fuels* **27**, 1141–1150 (2013).
- <sup>29</sup>Z. Huang, M. Zhao, Y. Xu, G. Li, and H. Zhang, "Eulerian-Lagrangian modeling of detonative combustion in two-phase gas-droplet mixtures with OpenFOAM: Validations and verifications," *Fuel* **286**, 119402 (2021).
- <sup>30</sup>A. Dasgupta, E. Gonzalez-Juez, and D. C. Haworth, "Flame simulations with an open-source code," *Comput. Phys. Commun.* **237**, 219–229 (2019).
- <sup>31</sup>L. F. Gutiérrez Marcantoni, J. Tamagno, and S. Elaskar, "rhoCentralRfFoam: An OpenFOAM solver for high speed chemically active flows—Simulation of planar detonations," *Comput. Phys. Commun.* **219**, 209–222 (2017).
- <sup>32</sup>C. Li, K. Kailasanath, and E. Oran, "Effects of boundary layers on oblique-detonation structures," in 31st Aerospace Sciences Meeting, 1993.
- <sup>33</sup>S. Miao, D. Xu, T. Song, and J. Yu, "Shock wave-boundary layer interactions in wedge-induced oblique detonations," *Combust. Sci. Technol.* **192**, 2345–2370 (2020).
- <sup>34</sup>K. Mazaheri, Y. Mahmoudi, and M. I. Radulescu, "Diffusion and hydrodynamic instabilities in gaseous detonations," *Combust. Flame* **159**, 2138–2154 (2012).
- <sup>35</sup>D. R. Stull and H. Prophet, *JANAF Thermochemical Tables*, 2nd ed. (U.S. National Bureau of Standards, 1971).
- <sup>36</sup>C. K. Law, *Combustion Physics* (Cambridge University Press, 2006).
- <sup>37</sup>G. Strang, "On the construction and comparison of difference schemes," *Siam J. Numer. Anal.* **5**, 506–517 (1968).
- <sup>38</sup>M. Y. Hussaini, B. V. Leer, and J. V. Rosendale, *Upwind and High-Resolution Schemes* (Springer-Verlag, Heidelberg, 1997).
- <sup>39</sup>W. Xie, R. Zhang, J. Lai, and H. Li, "An accurate and robust HLLC-type Riemann solver for the compressible Euler system at various Mach numbers," *Int. J. Numer. Methods Fluids* **89**, 430–463 (2019).
- <sup>40</sup>Q. Yang, P. Zhao, and H. Ge, "reactingfoam-SCI: An open source CFD platform for reacting flow simulation," *Comput. Fluids* **190**, 114–127 (2019).
- <sup>41</sup>Shock and Detonation Toolbox (SDT), see <https://shepherd.caltech.edu/EDL/PublicResources/sdt> for the introduction and help documents for SDT.
- <sup>42</sup>Z. Zhang, C. Wen, W. Zhang, Y. Liu, and Z. Jiang, "A theoretical method for solving shock relations coupled with chemical equilibrium and its applications," *Chin. J. Aeronaut.* **35**, 47–62 (2022).
- <sup>43</sup>G. Ben-Dora, M. Ivanov, E. I. Vasilev, and T. Elperin, "Hysteresis processes in the regular reflection-Mach reflection transition in steady flows," *Prog. Aerosp. Sci.* **38**, 347–387 (2002).
- <sup>44</sup>J. D. Anderson, *Fundamentals of Aerodynamics* (McGraw Hill Higher Education, 2001).
- <sup>45</sup>G. BenDor, O. Iggra, and T. Elperin, *Handbook of Shock Waves* (Cambridge University Press, 2000).